



# Grain-Boundary-Free Glassy Solid Electrolytes based on Sulfide Materials: Effects of Oxygen and Nitrogen Doping on Electrochemical Performance

Ran Zhao,<sup>[a]</sup> Guantai Hu,<sup>[a]</sup> Steven Kmiec,<sup>[a]</sup> Jacob Wheaton,<sup>[a]</sup> Victor M. Torres, III,<sup>[a]</sup> and Steve W. Martin<sup>\*[a]</sup>

While much of the current research on glassy solid electrolytes (GSEs) has focused on the binary  $\text{Li}_2\text{S} + \text{P}_2\text{S}_5$  system, compositions with Si are of interest because Si promotes stronger glass formation and allows low-cost melt-quenching (MQ) synthesis under ambient pressure. Another advantage is that they can be formed in homogeneous and continuous glass forms, as a result they are free of grain boundaries. In this work, we have examined the structures and electrochemical properties of bulk glass pieces of sulfide and oxy-sulfide GSE compositions and have also expanded the study by using LiPON glass as a dopant to produce an entirely new class of nitrogen doped mixed oxy-

sulfide nitride (MOSN) GSEs. Upon doping with oxygen and nitrogen, the solid electrolyte interface (SEI) is stabilized and the doped MOSN GSE exhibits a critical current density (CCD) of  $1.8 \text{ mA cm}^{-2}$  at  $100^\circ\text{C}$ . We also report on improving the glass quality, the SEI engineering and its limitations, and future plans of improving the electrochemical performance of these homogeneous MQ MOSN GSEs. These fundamental results can help to understand the structures and doping effects of the bulk GSEs, and as such can provide a guide to design improved homogeneous grain-boundary-free GSEs.

## Introduction

Sulfide-based solid electrolytes (SEs) have been shown to have high ionic conductivities, low electronic conductivities, excellent thermal and mechanical properties and as such are considered as promising options for the next generation of all-solid-state rechargeable lithium (and sodium) metal batteries. The utilization of a non-flammable inorganic SE and lithium metal (LM) anode are seen as viable pathways to significantly improve the safety and increase the specific energy of the batteries.

The sulfide-based SEs have been studied for more than four decades<sup>[1–4]</sup> and high lithium-ion conductivities have been achieved in all the three categories of materials: crystalline, glass-ceramic, and glass. The crystalline sulfide SEs, for instance,  $\text{Li}_{10}\text{SiP}_2\text{S}_{11.3}\text{O}_{0.7}$  (LSIPS),<sup>[5]</sup>  $\text{Li}_{10}\text{GeP}_2\text{S}_{12}$  (LGPS)<sup>[6]</sup> and  $\text{Li}_{9.54}\text{Si}_{1.74}\text{P}_{1.44}\text{S}_{11.7}\text{Cl}_{0.3}$  (LSPS–Cl)<sup>[7]</sup> were synthesized by a combination of planetary ball-milling (PBM) and elevated temperature solid-state reaction, and achieved high conductivities of  $3.1$ ,  $12$  and  $25 \text{ mS cm}^{-1}$ , respectively, at  $25^\circ\text{C}$ . Sulfide glass-ceramic SEs can be either produced by melt-quenching (MQ)

followed by a heat treatment above the crystallization temperature ( $T_c$ )<sup>[8,9]</sup> or by precipitation of crystalline phases from the glassy sulfide materials made by PBM.<sup>[10,11]</sup> Among the most studied are the glass-ceramic  $\text{Li}_2\text{S} + \text{P}_2\text{S}_5$  (LPS) phases which exhibit a conductivity over  $1 \text{ mS cm}^{-1}$ , while the original LPS glassy SE (GSEs) themselves showed a lower conductivity of  $0.1 \text{ mS cm}^{-1}$ .<sup>[10]</sup> Recently, Nazar et al. reported a lithium oxy-thioborosilicate GSE with a conductivity of  $2 \text{ mS cm}^{-1}$ .<sup>[12]</sup> For the synthesis of GSEs, the more widely used method is still high energy PBM since the technique is relatively easy and has the potential to be scaled to the kg and greater levels. MQ, on the other hand, requires high temperatures of  $\sim 1,000^\circ\text{C}$  and in some cases, like the thiophosphates, pressure control.

Though high conductivities have been achieved in various sulfide-based GSEs, the practical application of the pure sulfide SEs in LM batteries is limited by these SEs' inability to effectively suppress the formation of lithium dendrites (LDs). Once LDs grow across the SEs, typically forming at and above the critical current density (CCD) or after cycling for long periods of time, the battery will short. Among many studies of LDs forming through SEs, Carter and Chiang et al. have investigated the LD penetration through inorganic SEs and found that 'pre-existing flaws produces crack-tip stresses which drive crack propagation' and the 'lithium infiltration depends on solid-state electrolyte surface morphology, in particular the defect size and density'.<sup>[13]</sup> Consistent with these findings, the cycle life and CCD are limited in garnet type polycrystalline SEs due to the short-circuit caused by LD formation along the grain boundaries and voids in these polycrystalline ceramics.<sup>[14,15]</sup> These authors observed that the MQ LPS GSE had the largest CCD, approaching  $11 \text{ mA cm}^{-2}$  of the crystalline, glass-ceramic and glassy SEs they measured and concluded that the intrinsic

[a] R. Zhao, G. Hu, S. Kmiec, J. Wheaton, V. M. Torres, III, S. W. Martin  
Department of Materials Science and Engineering,  
Iowa State University,  
Ames, IA 50010, United States  
E-mail: s.wmartin@iastate.edu

 Supporting information for this article is available on the WWW under  
<https://doi.org/10.1002/batt.202100356>

 © 2022 The Authors. *Batteries & Supercaps* published by Wiley-VCH GmbH.  
This is an open access article under the terms of the Creative Commons Attribution Non-Commercial NoDerivs License, which permits use and distribution in any medium, provided the original work is properly cited, the use is non-commercial and no modifications or adaptations are made.

defect-free nature of the LPS GSE was a root to enabling the significantly higher CCD than the crystalline and partially crystalline glass-ceramic SEs. As discussed in these previous studies, to minimize the surface energy, metal ions tend to accumulate on the nuclei and the nuclei start to grow into particles. Subsequent ions then prefer to aggregate on the tips of these pre-existing particles with increasing current density. In the case of SEs with surface defects and particle boundaries, this nucleation will be uneven, and these defects and boundaries will accumulate ion aggregations. In a grain-boundary-free morphology, such as MQ GSEs, without the surface defects and grain boundaries in the bulk electrolyte, the formation of LDs may be suppressed. However, while these results are promising, they were demonstrated on SE samples whose electrode areas were only a few  $\mu\text{m}^2$  and as such, these results have, so far to our knowledge, not been demonstrated on larger, more realistic, areas of a few  $\text{cm}^2$  and larger. The testing of the hypothesis that defect-free MQ GSEs will enable higher CCDs than crystalline and or partially crystalline SEs is one of the aims of our study here.

For the sulfide-based materials, grain-boundary-free bulk homogeneous glass samples can be synthesized by traditional MQ methods so long as the compositions can be optimized to enable sufficient undercooling. It is noted that among the three groups of sulfide-based SEs described above, only glassy materials can be melted into bulk homogeneous grain-boundary-free pieces. Polycrystalline ceramic and glass-ceramic SEs, on the other hand, are formed by ceramic processing of starting material powders that necessarily result in multi-grained SEs.

Though some of these polycrystalline sulfide SEs show the highest conductivities, there are disadvantages and limitations in their practical application: first, the lithium penetration of the SE not only depends on the material properties, but is also influenced by the pellet quality and the surface morphology.<sup>[16]</sup> To make uniform pellets, the particle size and pressing conditions need to be very carefully controlled. In addition, the area of the SE is limited by the pressing equipment, and the quality of the pellet is hard to maintain when processed at the large scale required to achieve low cost. In turn, this means that these polycrystalline SEs may only be good candidates for small portable electronic devices. These concerns can be solved by the utilization of SEs in the glassy form, GSEs. In the homogeneous single-phase GSEs which can be used as-synthesized, the interphase grain-boundary vanishes and the amount of thin GSEs can be scaled to metric ton levels and little to no pressing procedures need to be done. While the conductivities of the GSEs are not yet as high as some of the better polycrystalline phases,  $\sim 1 \text{ mScm}^{-1}$  compared to  $\sim 10 \text{ mScm}^{-1}$  at 25 °C, the practical application of the GSEs is still promising because the thickness of the GSE can be significantly reduced by pulling them into thin films down to 10  $\mu\text{m}$ . Such thin GSEs will have area resistances very comparable to those of the thicker pellet SEs.

The most widely studied GSEs are  $\text{Li}_2\text{S} + \text{P}_2\text{S}_5$  lithium thiophosphate (LPS) glasses and their lithium halide-doped analogs, which show  $\text{Li}^+$  conductivities as high as

$1 \text{ mScm}^{-1}$ .<sup>[17–20]</sup> However, to achieve the desired stoichiometry, the LPS glass must be synthesized in a sealed vitreous quartz ampoule due to the high vapor pressure of  $\text{P}_2\text{S}_5$ . So, for this GSE, MQ cannot be readily or easily used and hence PBM is still the preferred synthesis technique for many workers. Furthermore, many other GSE compositions in this field have been prepared and studied due to the simplicity in handling these often very reactive materials. To achieve MQ synthesized bulk glass samples under ambient pressures using open crucibles, the compositions need to be improved to reduce the vapor pressure and increase the resistance to crystallization of the undercooled melt. We and others have observed that the addition of a second glass former, such as Si, dramatically improves glass formation, reduces vaporization to  $\leq 1 \text{ wt\%}$  and enables bulk GSEs to be formed in thicknesses approaching 1 cm. Such compositions will allow greater flexibility in synthesis of GSEs.<sup>[21,22]</sup>

The lithium thiosilicate ( $\text{LiSiS}$ ) GSE and its analogs were first studied in 1985 when Kennedy et al. reported on  $\text{LiSiS}$ -based GSEs and their  $\text{LiI}$ - and  $\text{LiBr}$ -doped versions. These  $\text{LiSiS}$  GSEs had room temperature  $\text{Li}^+$  conductivities on the order of  $0.1 \text{ mScm}^{-1}$ .<sup>[23]</sup> Though synthesized by MQ, these GSEs were still tested in the pellet format due to the non-melt cast and fractured shard shape of the as-made glasses. In this work, we also chose  $\text{SiS}_2$  as a glass co-former and GSEs were successfully synthesized under ambient pressure and open crucibles, quenched into disc-shaped molds, and their electrochemical properties were directly studied on the polished disc glass pieces.

Another important property of SEs is their electrochemical stability window vs. LM. It is well known that most sulfide-based GSEs have a limited thermodynamic electrochemical stability window between 1.7–2.1 V which limits their practical application.<sup>[24,25]</sup> Therefore, the formation of a stabilized SEI is critical to achieve the stability between the GSE and LM.<sup>[26–29]</sup> One method to stabilize the interface is to alter the composition of the SEs. In addition to sulfide-based GSEs, pure oxide and nitride SEs have also been investigated, but have poor electrochemical properties: the conductivity of pure oxide GSEs is too low to be used in batteries;<sup>[3]</sup> despite pure  $\text{Li}_3\text{N}$  having a sufficient conductivity of  $1.2 \text{ mScm}^{-1}$  at room temperature, its low decomposition voltage of 0.445 V makes it impossible to be used as a SE.<sup>[30]</sup> However, substituting the larger and more polarizable sulfide ions for oxide or nitride ions has proven to be a successful method to improve the electrochemical properties of GSEs. For example, Kondo et al. reported on a  $\text{Li}_3\text{PO}_4$ -doped  $\text{LiSiS}$  GSE which exhibited superior stability in contact with LM anodes.<sup>[31]</sup> Further, Tatsumisago et al. claimed that  $\text{Li}_3\text{N}-\text{SiS}_2$  and  $\text{Li}_3\text{N}$  doped  $\text{LiSiS}$  GSEs have improved electrochemical properties and exhibited high electrochemical stability over a wide potential range of 0 to +10 V.<sup>[32,33]</sup> However, none of these previous works utilized grain-boundary free glasses as SEs, but rather pressed powders of the MQ composition. To our knowledge, very little if any systematic study has been made on MQ GSEs comprising a mixed glass former (MGF), P and Si, and mixed oxy-sulfide-nitride (MOSN) anions when processed into a homogeneous

bulk glass MQ sample that is free of heterogeneities and defects such as grain boundaries. It is the purpose of this study then to examine the structure, properties, and electrochemical behavior of this new class of MQ MGF MOSN GSEs

In the one study that appears to concern grain-boundary free homogeneous GSEs by Porz et al.,<sup>[13]</sup> these workers observed that a MQ LPS glass exhibited the highest resistance to LD penetration of  $10 \text{ mA cm}^{-1}$  compared to less than  $5 \text{ mA cm}^{-1}$  for polycrystalline LPS and LLZTO garnet SEs. However, a significant limitation of this study was that the area examined was only a few  $\mu\text{m}^2$  and the total current passed was in the  $\mu\text{A}$  range. Hence, while important from a materials performance perspective, it appears that to date there has been no effort to investigate if these high CCDs of  $10 \text{ mA cm}^{-1}$  can be realized in the  $\text{cm}^2$  area and  $10 \text{ s}$  of  $\text{mAh cm}^{-1}$  areal capacity necessary for functional solid-state batteries. It is to this challenge that the present paper is directed.

In this work, we adopted the doping strategy to achieve significantly improved interfacial stability of the GSE in contact with LM by partial and systematic substitution of the sulfide anion with oxide and nitride anions. Perhaps unique to our research laboratory, we are capable of preparing grain-boundary free bulk GSE pieces to be directly characterized as SEs. In this first report on these GSEs, three different compositions were successfully prepared by the MQ method: the pure sulfide GSE as a base composition with the composition  $0.6 \text{ Li}_2\text{S} + 0.4(0.8 \text{ SiS}_2 + 0.2 \text{ P}_2\text{S}_5)$  named as LPS; an oxy-sulfide GSE of the composition  $0.67 \text{ Li}_2\text{S} + 0.33(0.8 \text{ SiS}_2 + 0.2 \text{ P}_2\text{O}_5)$  named as LPSO; and a LiPON doped oxy-sulfide GSE with the composition  $0.95(0.67 \text{ Li}_2\text{S} + 0.264 \text{ SiS}_2 + 0.066 \text{ P}_2\text{O}_5) + 0.05(\text{LiPO}_{2.20}\text{N}_{0.54})$  named as LPSON. The amorphous nature of the samples was investigated with X-ray diffraction (XRD). The SRO structures were analyzed using Raman and  $^{31}\text{P}$  and  $^{29}\text{Si}$  MAS NMR spectroscopies. Symmetric cells were assembled from the GSEs in a structure of Li/GSE/Li, and galvanostatic cycling was performed to test the stability of the GSE upon cycling with LM.

$0.05(\text{LiPO}_{2.20}\text{N}_{0.54})$  named as LPSON. The amorphous nature of the samples was investigated with X-ray diffraction (XRD). The SRO structures were analyzed using Raman and  $^{31}\text{P}$  and  $^{29}\text{Si}$  MAS NMR spectroscopies. Symmetric cells were assembled from the GSEs in a structure of Li/GSE/Li, and galvanostatic cycling was performed to test the stability of the GSE upon cycling with LM.

## Results and Discussion

### XRD characterization and SEM imaging

As expected, all the glass samples appear amorphous in the powder XRD (PXRD) patterns as shown in Figure 1A, no diffraction peaks for any crystalline phases were observed. We have studied sulfide and oxy-sulfide GSEs made by PBM in our previous work,<sup>[34,35]</sup> and these PBM GSEs with compositions similar to those of LPS and LPSO showed diffractions associated with unreacted crystalline  $\text{Li}_2\text{S}$  and so-called ejected Si from the  $\text{SiS}_2$  in their PXRD patterns. Comparing the results from our previous work and this study, the MQ method appears to be superior, and produces more homogeneous and higher purity GSE materials.

The photos and morphologies of polished glass surfaces are shown in Figure 1(B–D). All of the GSE samples are transparent and clear with different colors. The LPS glass appeared to be a light-yellow glass, while the oxygen doped LPSO glass displayed an orange color. With only about 1 wt% nitrogen replacement in the networking atoms ( $\text{N}/(\text{O}+\text{S})$ ) in the LPSON

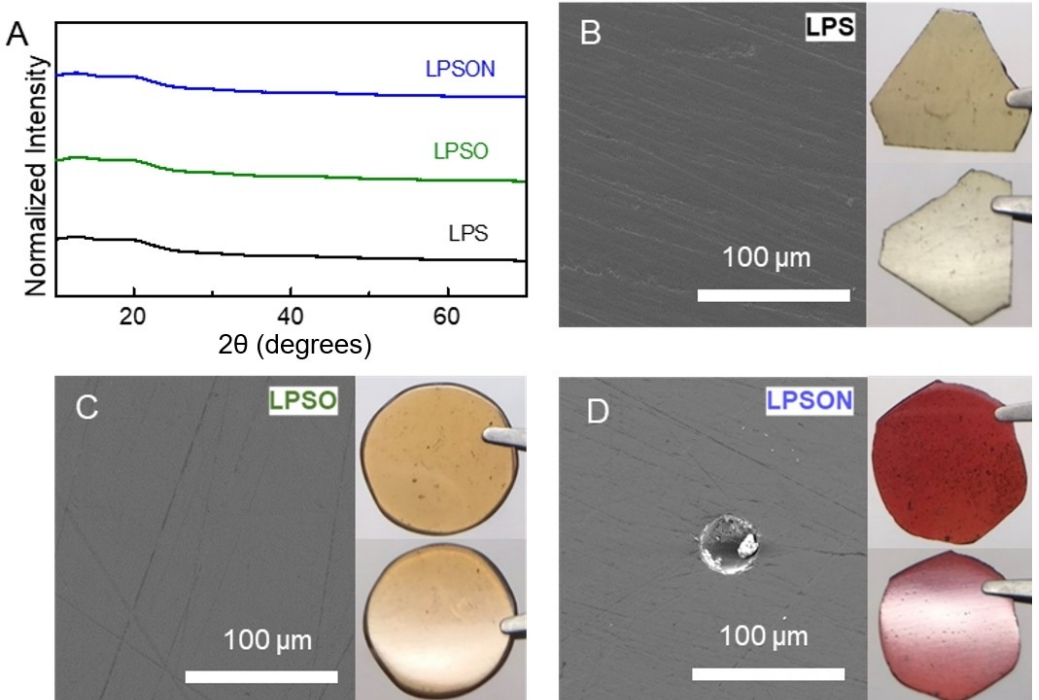


Figure 1. A) PXRD patterns of LPS, LPSO and LPSON glasses. SEM images (left) and photos (right) of polished glasses: B) LPS, C) LPSO, and D) LPSON.

GSE, the glass color changed dramatically to cardinal red. We need to note that small dark spots were observed in all the glasses especially in the LPSON sample. Instead of being impurities, the dark spots were small gas bubbles trapped inside the glass that appear to be created during MQ. For such bubbles close to the glass surface, holes exposed by polishing can be seen clearly on the surface both in the SEM image and also by eye when the light shines on the LPSON glass piece as shown in Figure 1(D). There are two reasons for the increased amount of micro-bubbles in the LPSON samples. First, thermal decomposition of LiPON generates N<sub>2</sub> during the high temperature melting, resulting in trapped N<sub>2</sub> bubbles in the glass. Secondly, the viscosity of LPSON melt was significantly higher than that of the LPS and LPSO melts and when pouring the melted LPSON glass liquids onto the brass plates, the high viscosity trapped bubbles in the glass caused by the casting process.

Though scratches made by polishing and tiny holes arising from trapped gas in the starting material glass powder can be observed in the SEM images of polished glass surfaces (Figure 1B–D), the grain-boundaries and large porous structures, which are common in the pressed pellet GSEs, cannot be seen on the glass surfaces. It is this grain-boundary-free morphology that is believed to suppress the formation of LDs.

### Short range order of the MQ GSEs

To characterize and follow the chemical changes taking place in the short-range order (SRO) structures of these different GSEs with different networking atoms studied in this work, Raman and <sup>31</sup>P and <sup>29</sup>Si MAS NMR spectroscopies were performed on these GSEs. The different P–S and Si–S SRO structural units present in Li–P–S GSEs and Li–Si–S GSEs are shown in Figure S2.

The Raman spectra are shown in Figure 2. In the low wavenumber region,  $< 500 \text{ cm}^{-1}$ , the strongest modes have been attributed mainly to vibrational modes of the (SiS<sub>4</sub>)<sup>4-</sup> (Si<sup>0</sup>) and (PS<sub>4</sub>)<sup>3-</sup> (P<sup>0</sup>), where in the latter shorthand notation, the superscript refers to number of bridging sulfur (or oxygen) anions in the SRO structures. The LPS composition shows two dominate peaks at 423 cm<sup>-1</sup> and 388 cm<sup>-1</sup>. The first mode has been assigned to (PS<sub>4</sub>)<sup>3-</sup> symmetric stretch in the P<sup>0</sup> SRO,<sup>[36–38]</sup> whereas the latter we believe to be associated with P–S symmetric stretch in the P<sup>1P</sup> SRO (P<sub>2</sub>S<sub>6</sub>)<sup>4-</sup>, and with the Si–S symmetric stretch in Si<sup>0</sup> SRO (SiS<sub>4</sub>)<sup>4-</sup>.<sup>[36–40]</sup> Since the Si–S and P–S bonding vibrations are highly overlapped in the wavenumber range from 360 cm<sup>-1</sup> to 450 cm<sup>-1</sup>, the specific SRO structures cannot be uniquely identified through the Raman spectra alone. In the oxygen- and oxygen/nitrogen doped glasses, LPSO and LPSON, the dominant peaks at 388 cm<sup>-1</sup> decrease in intensity.

In the higher Raman wavenumber region  $> 500 \text{ cm}^{-1}$ , peaks in the range of 500–650 cm<sup>-1</sup> for the LPS GSE are attributed to the symmetric stretch of P=S bonds.<sup>[36,38]</sup> In the Raman spectra of the oxygen-doped LPSO GSE, new peaks at 970 cm<sup>-1</sup> and 1100 cm<sup>-1</sup> are observed and are associated with non-bridging

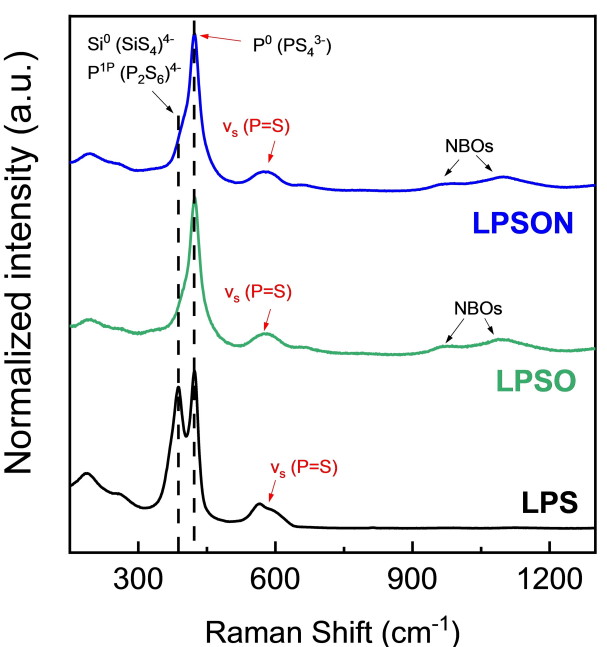
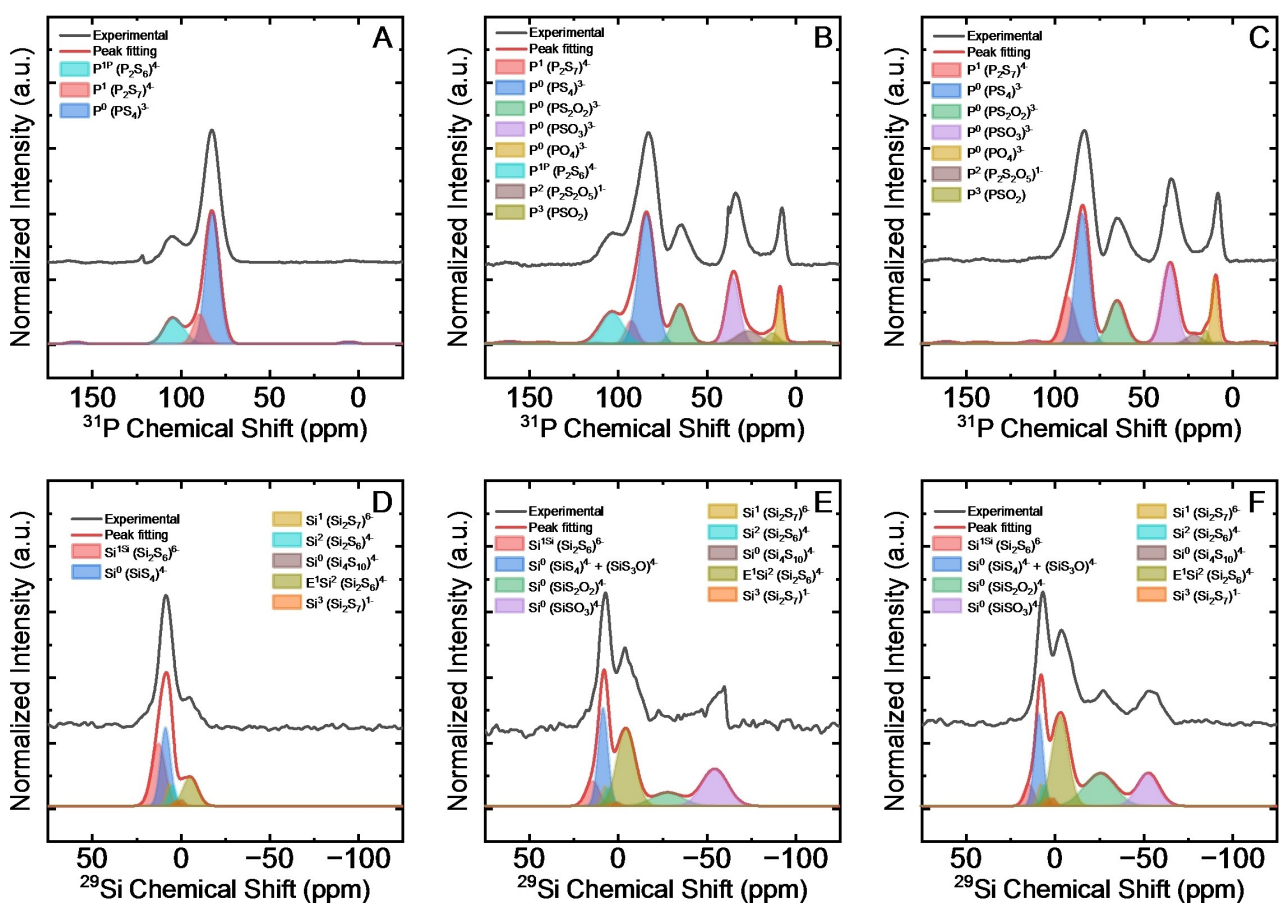


Figure 2. Raman spectra of LPS, LPSO and LPSON MQ GSEs.

oxygens (NBOs) bonding to P and Si, such as  $\equiv\text{P}-\text{O}^{-1}$  and  $\equiv\text{Si}-\text{O}^{-1}$ , respectively.<sup>[36,41,42]</sup> The Raman scattering intensities of modes associated with these oxide SRO species are significantly lower than those associated with sulfide species due to both their lower overall concentration in the samples and the much lower polarizability of oxide SRO species compared those of the oxide SRO species.

The <sup>31</sup>P MAS NMR spectra of the three MQ GSEs and their deconvolutions are given in Figure 3(A–C). In the pure sulfide GSE, LPS, the <sup>31</sup>P MAS NMR spectra consists of three peaks which have been assigned to the SRO units containing only P and S, P<sup>1P</sup> (P<sub>2</sub>S<sub>6</sub>)<sup>4-</sup> at 105 ppm, P<sup>1</sup> (P<sub>2</sub>S<sub>6</sub>)<sup>4-</sup> at 89 ppm, and P<sup>0</sup> (PS<sub>4</sub>)<sup>3-</sup> at 82 ppm.<sup>[36,37,43–45]</sup> With oxygen substitution in LPSO and LPSON, as expected, new SRO units containing a mixture of S and O and pure O are observed. Further, and as expected, the <sup>31</sup>P MAS NMR spectra of LPSO and LPSON are quite similar, except for one main difference, the peak at 105 ppm (assigned to P<sup>1P</sup>) remains in the spectra for LPSO but disappears in the spectra for LPSON. The loss of the P<sup>1P</sup> peak in the LPSON spectrum appears to be due to the introduction of nitrogen species through the LiPON doping. Due to the small N concentration in the LPSON GSE, direct P (or Si) MAS NMR evidence cannot be found for the presence of P–N species. However, as will be seen below in the N1s XPS spectra, the presence of LiPON in LPSON promotes the creation of tri-coordinated di-coordinated P=N=P bridging nitrogen (BN) atoms that may be preferentially inserting into the covalent P–P bonds of the P<sup>1P</sup> SRO units. At this point, it is not known why the added O through LiPO<sub>3</sub> does not equally replace these P–P bonds in the P<sup>1P</sup> SRO units. It may be that O is not a sufficiently strong Lewis base. We will address this question more fully below in discussing the XPS spectra of these GSEs.



**Figure 3.** Deconvoluted <sup>31</sup>P MAS NMR spectra of A) LPS, B) LPSO, and C) LPSON GSEs. Deconvoluted <sup>29</sup>Si MAS NMR spectra of D) LPS, E) LPSO, and F) LPSON GSEs.

With the added O from the P<sub>2</sub>O<sub>5</sub> in the LPSO and the combination of P<sub>2</sub>O<sub>5</sub> and LiPON in LPSON GSEs, new peaks centered at 7.7 ppm, 34 ppm, and 64 ppm are observed in the spectra of both LPSO and LPSON and are assigned to the presence of the P<sup>0</sup> SRO units (PO<sub>4</sub>)<sup>3-</sup>, (PO<sub>3</sub>S)<sup>3-</sup>, and (PO<sub>2</sub>S<sub>2</sub>)<sup>3-</sup>, respectively.<sup>[44-46]</sup> Weak intensity peaks at 12 ppm and 25 ppm are tentatively assigned to the presence of P<sup>1</sup> (P<sub>2</sub>S<sub>2</sub>O<sub>5</sub>)<sup>2-</sup> and P<sup>2</sup> (PSO<sub>2</sub>)<sup>-</sup> SRO species. Finally, very weak intensity peaks are observed at ~125 ppm and ~35 ppm in the LPS and LPSO spectra, respectively, and these are attributed to SRO species contained in a small volume, <1%, of these samples that have partially crystallized in the sample. A detailed listing of all of the peak positions and fitting parameters can be found in Table S1 and Figures S1 and S2.

The <sup>29</sup>Si MAS NMR spectra of the MQ LPS, LPSO, LPSON GSEs are shown in Figure 3(D-F). In the pure sulfide LPS GSE, the Si MAS NMR spectrum is defined by 3 main resonances at 11.5 ppm, 7.5 ppm, and -6.3 ppm, but four additional weaker resonances can be clearly observed after deconvolution and are centered at 5.5 ppm, 3.6 ppm, 0.5 ppm, and -1.5 ppm. In previous <sup>29</sup>Si NMR studies of LSIS glasses, Eckert et al. have attributed resonances in the chemical shift regions of 4 to 8 ppm to corner sharing Si-S groups, see Figure S1, and assigned the resonances in the chemical shift region between -6 and -12 ppm to edge-sharing Si-S units, again see

Figure S1. Therefore, we attribute the more intense peaks 11.5 ppm, 7.5 ppm and -6.3 ppm to (Si<sub>2</sub>S<sub>6</sub>)<sup>6-</sup> (Si<sup>1Si</sup>)<sup>4-</sup> (Si<sup>0</sup>), and (Si<sub>2</sub>S<sub>6</sub>)<sup>4-</sup> (E<sup>1</sup>Si<sup>2</sup>) SRO units, respectively, using the edge sharing (E<sup>i</sup>) notation SRO notation of Eckert et al. where the superscript i is the number of tetrahedron edges shared.<sup>[44-48]</sup> Weaker intensity peaks are associated to the SRO units (Si<sub>4</sub>S<sub>10</sub>)<sup>4-</sup> (Si<sup>3M</sup>) at -1.5 ppm, (Si<sub>2</sub>S<sub>7</sub>)<sup>-</sup> (Si<sup>3</sup>) at 0.5 ppm, (Si<sub>2</sub>S<sub>6</sub>)<sup>4-</sup> (Si<sup>2</sup>) at 3.6 ppm, and (Si<sub>2</sub>S<sub>7</sub>)<sup>6-</sup> (Si<sup>1</sup>) at 6 ppm. These SRO units and their chemical shifts in LSIS GSEs have also been reported upon in the literature by others.<sup>[39,49,50]</sup> In addition, a systematic study of the GSEs in the Na<sub>2</sub>S + SiS<sub>2</sub> glass system by Watson et al. has also assigned the resonance located at 7 ppm to Si<sup>0</sup> (SiS<sub>4</sub>)<sup>4-</sup> and the resonance centered at -6.3 ppm to the edge-sharing units, E<sup>1</sup>Si<sup>2</sup> (Si<sub>2</sub>S<sub>6</sub>)<sup>4-</sup>.<sup>[39,40]</sup> However, due to the low <sup>29</sup>Si abundance, the <sup>29</sup>Si NMR spectra, Figure 3(D-F), are admittedly quite noisy even with the multiple day acquisitions used here and this leads to not only some ambiguity in peak assignments, but also to slight deviations between the calculated and experimental charge balance requirements between the amount of Li<sup>+</sup> positive charge and the Si and P SRO anion negative charges, see Table S1.

In the <sup>29</sup>Si MAS NMR spectra of the LPSO GSE, the substitution of P<sub>2</sub>O<sub>5</sub> for P<sub>2</sub>S<sub>5</sub> and the increase in Li<sub>2</sub>S concentration has a direct impact on the SRO structures present in these GSEs. In particular and as seen in the <sup>31</sup>P MAS NMR

spectra, the emergence of MOS silicon peaks can be observed at chemical shifts  $-29$  ppm and  $-56$  ppm. These resonances are attributed to the  $\text{Si}^0$  units of  $(\text{SiO}_2\text{S}_2)^{4-}$  and  $(\text{SiO}_3\text{S})^{4-}$ , respectively.<sup>[39,40,47,48,51,52]</sup> The  $\text{Si}^0$  SRO unit  $(\text{SiOS}_3)^{4-}$  overlaps the main  $\text{Si}^0$  unit  $(\text{SiS}^4)^{4-}$  peak at  $7.5$  ppm. As perhaps expected, the  $^{29}\text{Si}$  MAS NMR spectra of LPSON is very similar to that of LPSO, with nearly identical peaks in similar positions. However, a main difference is that there is an increase in the intensity of the peak associated to the  $(\text{SiS}_2\text{O}_2)^{4-}$  ( $\text{Si}^0$ ) SRO unit, indicating that the small addition of LiPON does impact the structure of the LPSON GSE. Peak positions and fitting parameters are given in Table S1 and Figures S1 and S2 are presented to offer additional information for the SRO species of LPS, LPSO, and LPSON.

### Effect of oxygen and nitrogen doping in glass transition and crystallization temperatures

Glass transition temperatures are sensitive to changes in the composition and SRO structure of glass.<sup>[37,53]</sup> For these reasons, DSC measurements were made on these GSEs to reveal the effect of composition and SRO structural changes in these glasses and to determine the glass working range of these glasses,  $\Delta T \equiv T_c - T_g$ , the temperature range above the  $T_g$  of the glass, but below the  $T_c$  of the supercooled liquid. The working range is of great practical importance in forming these GSEs into shapes requisite for use in all solid-state batteries. The working range is the range of temperatures that corresponds to the difference in temperatures where glass begins to transition into a viscoelastic supercooled liquid and where the supercooled liquid crystallizes into a (typically) polycrystalline solid.

Figure 4(A) shows the DSC scans of the LPS, LPSO and LPSON GSEs in the range of  $250^\circ\text{C}$  to  $450^\circ\text{C}$ . The  $T_g$ s and

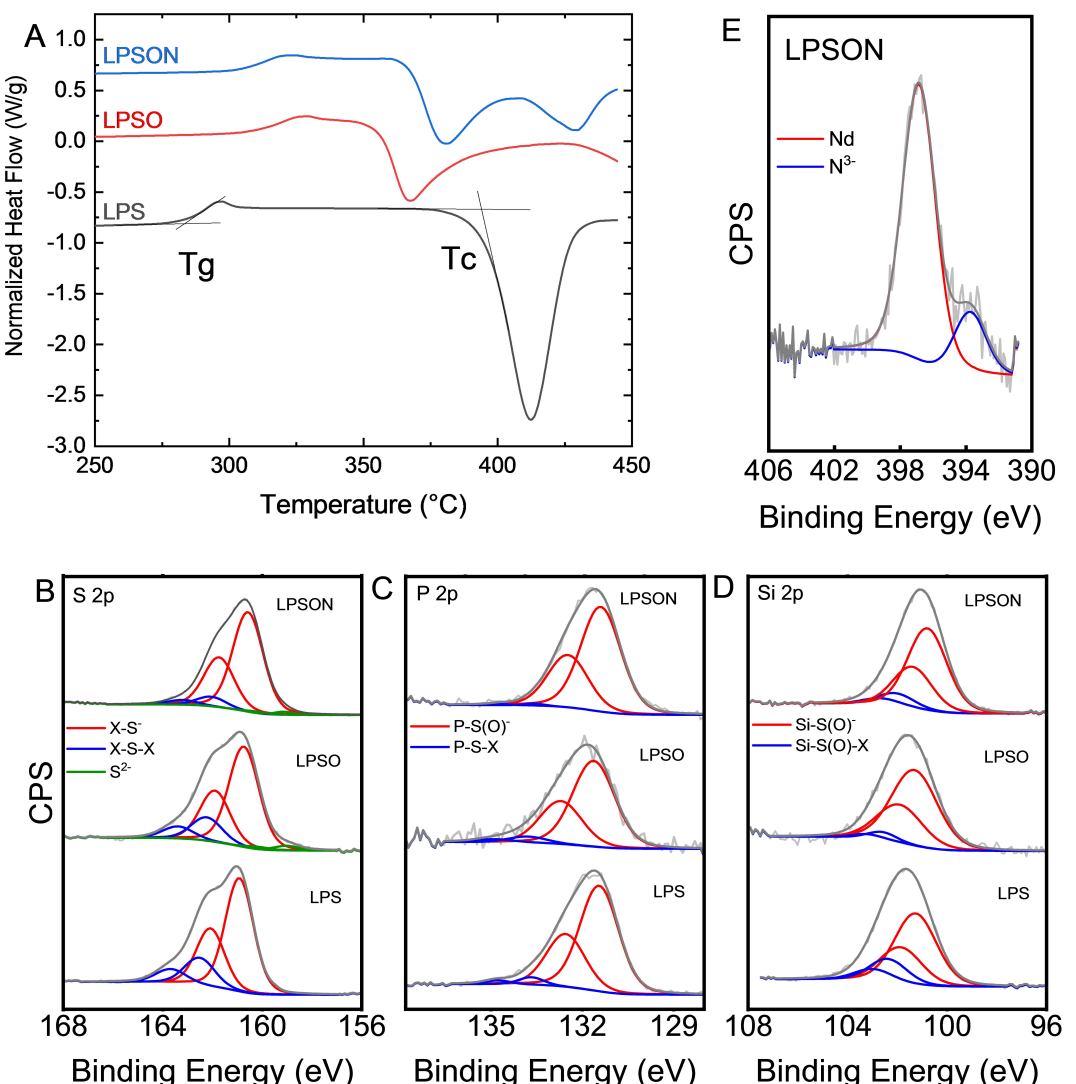


**Figure 4.** A) DSC heating scans of LPS, LPSO and LPSON GSEs. XPS spectra of B) S 2p, C) P 2p, D) Si 2p and E) N 1s for LPSON GSEs. No noticeable N1s signal was observed, as expected, for the LPS and LPSO GSEs and these are not shown for this reason.

working ranges, see the construction in Figure 4(A), are 283 °C and 112 °C for LPS, 308 °C and 48 °C for LPSO and 302 °C and 65 °C for LPSON, respectively, see Table S2. The smaller values for the glass transition temperatures for LPS compared to that of LPSO and LPSON is consistent with the presence of BOs in LPSO and the presence of BO and BN in LPSON. This effect appears to be more dominant over the fact that LPS has a lower modifier ( $\text{Li}_2\text{S}$ ) content, 60 mole%, than either LPSO or LPSON, 67 mole%. However, the BOs and BNs in LPSO and LPSON, which are absent in LPS, appear to not favorably influence the working range. These effects can be interpreted as the  $T_g$ , which is the temperature of the isoviscous point of  $10^{12}$  Poise, being controlled by the strength and number of the bridging bonds in the glass, here BO and BNs, whereas the crystallization of the supercooled liquid is controlled by the viscosity of the melt which is controlled by the overall network connectivity which is less in the more modified LPSO and LPSON GSEs. The addition of nitrogen in the LPSON GSE, however, does increase the working range by about 17 °C over that of LPSO, consistent with its higher network connectivity and numbers of BO and BNs. The tabulated values of  $T_g$ ,  $T_c$ , and  $\Delta T$  are reported in Table S2.

While all of the vibrational and NMR spectra of the LPSON GSE do not show direct evidence of the successful doping of N into the LPSON GSE, there is indirect evidence as indicated by the (slightly) increased working range described above. While the Raman spectra of LPSO and LPSON are nearly identical, the NMR spectra do show small systematic peak shifts and small differences in the peak intensity between LPSO and LPSON GSEs and the DSC thermograms exhibit systematic differences in the  $T_g$  and  $T_c$  values for all the three samples that are consistent with the incorporation of O and N in covalent BO and BN positions. The latter two results are the only evidence so far of the different structures of LPSO and LPSON. Since none of these results show direct evidence of nitrogen incorporation into LPSON, to further confirm the nitride substitution, XPS was performed on all three samples.

XPS measurements were performed to investigate the presence of N in the LPSON GSE and to examine the chemical bonding of the other elements in these GSE compositions. As shown in Figure 4(B), the high resolution XPS scans of the S2p region show the expected components of BS X—S—X and NBS X—S<sup>2-</sup> in all the three compositions, where X=P or Si.<sup>[54]</sup> S<sup>2-</sup> has only been found in a very limited amount in the higher modified LPSO and LPSON GSEs. Figure 4(C) shows the high resolution XPS scans of the P2p region. The P2p XPS spectra show four peaks corresponding to P2p<sub>3/2</sub> and P2p<sub>1/2</sub> in two chemical environments, which are assigned to non-bridging phosphorus (NBP), P—S<sup>2-</sup> or P—O<sup>-</sup>, and bridging phosphorus (BP), P—S—X, where X is Si or P, respectively. Similarly, Figure 4(D) presents the Si2p XPS spectra for the GSEs. Signals are attributed to non-bridging silicon (NBSi) and bridging silicon (BSi). The relative amounts of BSi and BP in LPS glass are slightly larger than that in LPSO and LPSON GSEs due to the lower concentration of  $\text{Li}_2\text{S}$ , and this result agrees with the Raman and NMR spectra described above.

Nitrogen incorporation is observed in the N1s XPS spectrum of LPSON GSE as shown in Figure 4(E) (No noticeable N1s signals were observed for the LPS and LPSO GSEs, as expected, and are not shown for this reason). The N1s binding energies of the intense and weak peaks are consistent with doubly coordinated nitrogen (Nd), P—N=P, and a small amount of free N<sup>3-</sup> anions, respectively. This result confirms the N doping into LPSON glass has been successful. It will be seen in the discussion below that the improvement of the electrochemical properties of the LPSON GSE over that of the LPSO and LPS GSEs can be attributed to the N incorporation in the LPSON GSE.<sup>[55]</sup>

CV measurements were performed and analyzed to obtain information regarding the potential-dependent electrochemical reactions for these GSEs. When scanned from -1 V to 5 V vs. Li/Li<sup>+</sup> (Figure 5A), a cathodic current peak from -1 V to 0 V and an anodic current peak between 0 V and 1 V were observed in all of the GSEs, which correspond to lithium plating and stripping, respectively.<sup>[56-58]</sup> No other peaks were observed in the potential range up to 5 V, suggesting that the glasses have a wide electrochemical stability window up to 5 V.

To further investigate the reactions between all of these GSEs and LM, voltage profiles of CV measurements were collected from 0 V to 4 V. No significant peaks associated other reactions were observed. However, in our previous work on PBM LPS and LPSO compositions, peaks arising lithium reaction with Si or S have been found,<sup>[34]</sup> indicating that the MQ synthesis method provides more homogeneous and higher purity GSEs and for this reason is superior to PBM method.

### Symmetric cell tests

Both theoretical and experimental studies have demonstrated that phosphorous-based sulfide GSEs and glass-ceramic SEs have a limited thermodynamic electrochemical stability window that appears to be centered around ~1.7 to ~2.1 V vs. Li/Li<sup>+</sup>.<sup>[24,25,59]</sup> The decomposing products are  $\text{Li}_2\text{S}$  and  $\text{Li}_3\text{P}$  when in contact with LM.<sup>[24,25,54,60]</sup> It is of interest here to investigate whether the addition of oxygen (LPSO) and oxygen and nitrogen (LPSON) increases the electrochemical stability of these GSEs and to determine if there is interfacial reaction between these MQ GSEs and LM and as a result determine affect the overall battery performance.

To evaluate the stability of these GSEs in contact with LM, Li/GSE/Li symmetric coin cells were tested with EIS measurements. When tested in a symmetric lithium cell using time-dependent EIS measurements, the overall resistance of the cell will reflect the type and amount of interfacial processes and the formed components. Figure S3 shows the resistance of the cells utilizing the three different GSEs for the first 9.5 hours at open circuit voltage, and the result is summarized in Figure 5(E). The overall resistance of the cell using LPS as the SE increases with time, and is about 50 times larger than the assembled cell resistance after only 9 hours, indicating the interphase of LPS and LM is a reactive SEI, i.e. a mixed conducting interphase (MCI).<sup>[54,60]</sup> The MCI of LPS will grow

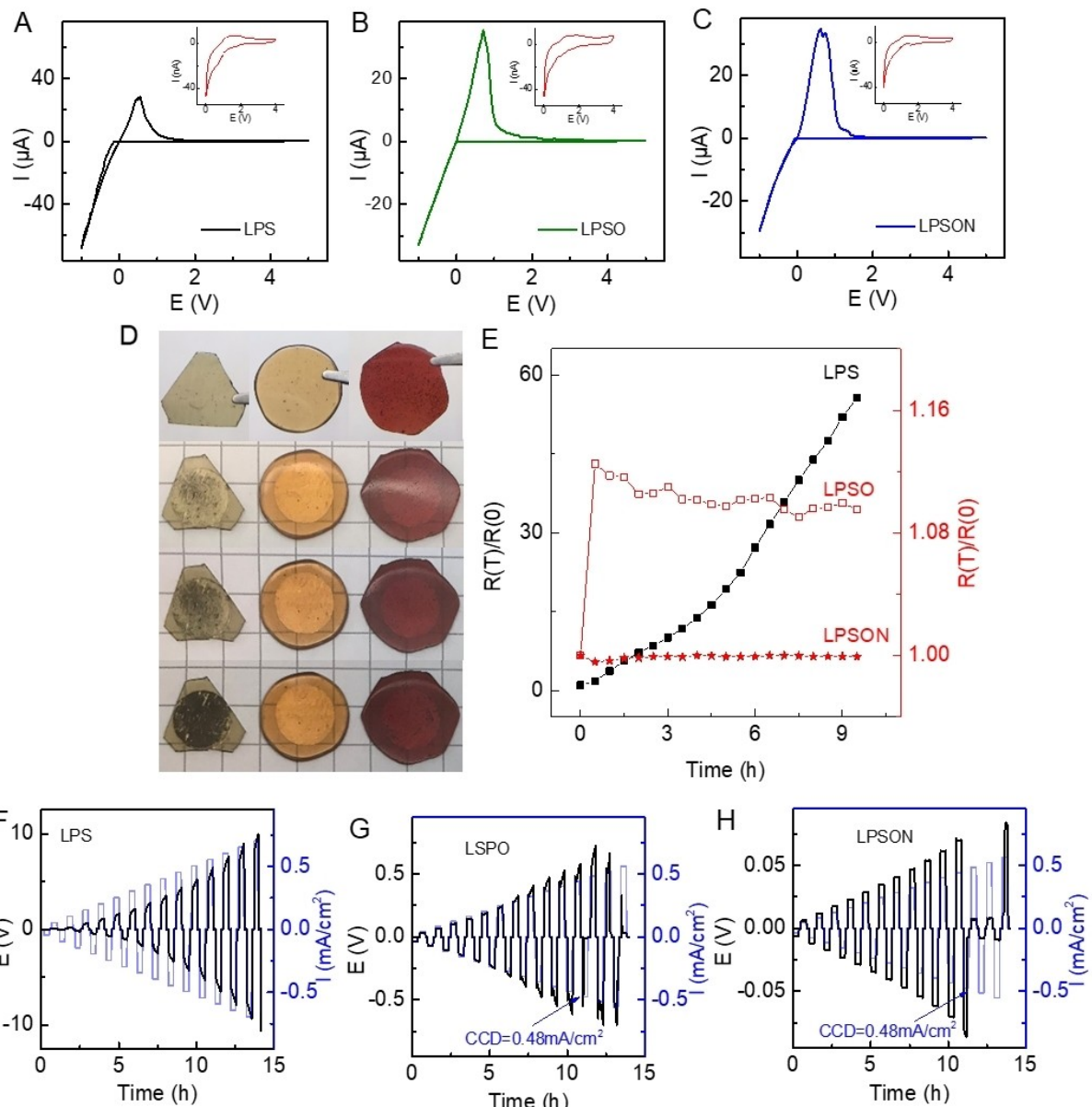


**Figure 5.** Cyclic voltammetry profiles from  $-1 \text{ V}$  to  $5 \text{ V}$  for A) LPS, B) LPSO, and C) LPSON GSEs. Inserted: voltage profiles scanned from  $0$  to  $4 \text{ V}$ . D) Color change of the glass/LM in glovebox with time. First: LPS, second: LPSO, third: LPSON. These photos are looking down through the transparent GSEs and onto the underlying LM/GSE interface. E) Relative resistance changes vs. time for MQ GSEs in Li/GSE/Li cells. Galvanostatic cycling of the Li/GSE/Li symmetric cells at step-increased current density at room temperature of F) LPS, G) LPSO, H) LPSON. The time for each step is  $20 \text{ min}$ ; the current intensity step size is  $0.04 \text{ mA cm}^{-2}$ .

across the GSE and eventually alters the properties of the GSE, which is in good agreement with our previous observation in the PBM LPS with a similar composition.<sup>[34]</sup> In the cell with LPSO as the SE, the overall resistance increased by 10% in the first 30 min. and but stabilized afterwards, suggesting the formation of a stable passivation SEI layer at the interface. Finally, for the MOSN GSE, LPSON, there is essentially no resistance change within this time window, which means that there is no significant interfacial reaction at the open circuit voltage. Note the use of the finer scale right y-axis for the LPSO and LPSON GSEs.

Another important test was done to reveal the reactivity of the glasses vs. LM. A clean LM foil piece was placed under each polished glass disc, and the interface could be easily seen through the transparent GSE. Pressure was applied carefully to ensure a good contact; pictures of the glasses and the interfaces were taken every two hours. As shown in Figure 5(D), there was a black layer growing with time in the interface of LPS and the LM foil, whereas in the other two glasses, no significant interfacial changes were observed, indicating LPSO and LPSON are more stable in contact with LM. These observations are consistent with the EIS results described above.

From the previous studies of Kennedy and Zhang,<sup>[61]</sup> the instability of  $\text{SiS}_2$ -based GSEs to LM may occur according to the reactions below:



In subsequent reaction (2), Li and Si will form a Li–Si alloy, which exhibits metallic behavior and conducts electrons.<sup>[62]</sup> Without a passivation layer, reactions (1) and (2) will eventually grow across the GSE and the properties of the GSE will be deteriorated. We believed that the addition of oxygen inhibits this reaction because as the Raman,  $^{29}\text{Si}$  and  $^{31}\text{P}$  MAS NMR, and XPS results show, the added oxygen bonds preferentially to the Si atom creating protective BOs on the Si atoms. Likewise, in extensive studies of Si-based anode materials reported in the literature, micrometer-sized  $\text{SiO}_2$  particles are known to be inactive with Li ions, while the nanometer-sized  $\text{SiO}_2$  reacts irreversibly with lithium.<sup>[63]</sup> As discussed in the Raman spectra and NMR sections, the addition of oxygen atoms generate Si and P MOS tetrahedra in the GSEs. As a result, we suggest here that the presence of the oxygen-rich Si and P tetrahedra inhibit the interfacial reaction of Si and P with Li. In general, it appears that the incorporation of oxygen is crucial to form a favorable and stable SEI layer when in contact with LM.

Likewise, Dudney and co-workers have long shown that N additions to Li–P–O phases to form the well-studied LiPON GSE completely passivates and stabilizes the LiPON/LM interface.<sup>[64]</sup> These authors report that similar to the strong BO bonds that form to the Si atoms, the strong P–N bonds that form in nitrogen doped LiPON equally protect the P from electrochemical reduction to  $\text{Li}_3\text{P}$  and other reduced species. While we have not conclusively shown that the added N to the LPSON GSE only bonds to the P, we have shown that the  $^{29}\text{Si}$  MAS NMR shows an increase in the population and intensity of the MOS peaks located at  $-54$  ppm and  $-27$  ppm. There appears to be no evidence of the formation of Si–N bonds in the  $^{29}\text{Si}$  MAS NMR spectra. Hence, we suggest here that the added O to the glass is bonded to the Si and therefore protects it against reduction by LM and the added N is preferentially bonded to P and therefore protects it against reduction by LM. The result of these two chemical protection schemas is that the LPSON GSE is electrochemically stable in contact with LM. Our observations here appear to be the very first results that show that GSE can be made essentially stable in contact with LM.

Temperature-dependent EIS was conducted on the LPS, LPSO, and LPSON GSEs to determine their room temperature ionic conductivities and the activation energy for conduction. The glasses were cast into discs, polished, and then sputtered with gold to create conformal blocking electrode contacts. Glasses were tested in a Novocontrol 2 dielectric spectrometer at a root-mean-square potential of  $0.5$  V in a frequency range from  $10$  MHz to  $0.1$  Hz. Samples were loaded into a cryostat and tested from  $-60$  to  $+90^\circ\text{C}$ . The Nyquist plots were fitted using a parallel resistor and constant phase element model with a Warburg utilized to model the space charge polarization

due to the blocking nature of the sputtered gold electrodes. The ionic conductivity data are shown in Figure 6. The activation energy was determined to be  $31.7 \pm 0.7$ ,  $32.1 \pm 0.4$ ,  $28.2 \pm 0.4 \text{ kJ mol}^{-1}$  for the LPS, LPSO, and LPSON GSEs, respectively. The room temperature ionic conductivities of the LPS, LPSO, and LPSON are  $(1.0 \pm 0.2) \times 10^{-3} (\Omega \text{ cm})^{-1}$ ,  $4.0 \times 10^{-4} (\Omega \text{ cm})^{-1}$ ,  $(6.6 \pm 0.4) \times 10^{-5} (\Omega \text{ cm})^{-1}$  respectively. From this data, it can be seen that the incorporation of oxygen and nitrogen reduces the conductivity of sulfide GSE, while the activation energy shows only minor changes that do not indicate a strong dependence of activation energy on the nitrogen and oxygen content in this system.

To further evaluate the electrochemical properties of these GSEs, Li/GSE/Li symmetric cells were then cycled at step-increased current densities at room temperature ( $\sim 18^\circ\text{C}$ ) as shown in Figure 5(F–H). A current density of  $0.04 \text{ mA cm}^{-2}$  was applied first, and then increased by  $0.04 \text{ mA cm}^{-2}$  for each cycle. After cycling for a few hours, the cells with LPSO and LPSON GSEs experienced a voltage drop to  $0$  V at a current density of  $0.48 \text{ mA cm}^{-2}$ , which is considered to be a result of LD formation through these GSEs. The current densities at which voltage drops and micro-shorts occur are considered to be the critical current densities (CCDs) for the LD formation in SEs. LPS did not short at lower voltages and currents, but rather as a result of the direction reaction of this GSE with LM to form a resistive SEI, this GSE reached the instrument limit,  $10$  V, before getting shorted. According to the ohm's law,  $R=V/I$ , since the  $V$  change is not linear, the overall resistance of the Li/LPS/Li cell is increasing with time, which is in good agreement of the EIS study. Since the LPS is not stable when cycling with LM, it is impossible to use LPS as a SE without further interfacial

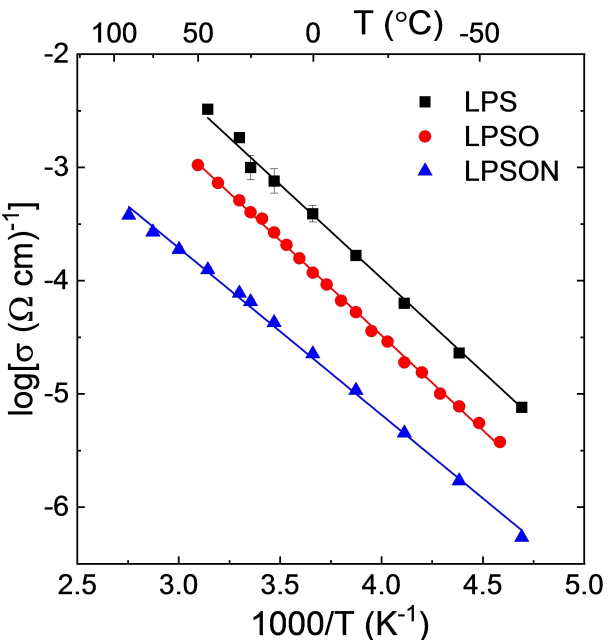


Figure 6. Temperature-dependent  $\text{Li}^+$  ion conductivity Arrhenius plots showing the conductivity of the LPS, LPSO, and LPSON GSEs. Error bars indicating the standard error of the conductivity measurements are hidden behind some of the symbols.

modification, even though for reasons not fully understood at this time, it appears to resist LD penetration better than LPSO and LPSON. For these reasons, we focus on LPSO and LPSON which generated stable SEIs, as shown above, when cycling with LM.

According to the SEM images and visual observations, bubbles were found in both LPSO and LPSON GSEs, especially on the surface of LPSON. The existence of the tiny bubbles reduced the actual contact area with LM and may also trigger the formation of LDs.<sup>[13]</sup> To improve the contact and also show the potential advantages of the grain-boundary free GSEs in high temperature application, we also tested the symmetric cells with LPSO and LPSON as SEs at 100 °C (Figure 7).

Both cells with LPSO and LPSON as SEs show an increased CCD at 100 °C, which indicates a better contact can suppress the LD growth, the Li/LPSO/Li and Li/LPSON/Li cells shorted at 1.2 and 1.76 mA cm<sup>-2</sup>, respectively. On closer investigation, the voltage of the cell increases beyond the linear relationship with time at a current of 0.4 mA cm<sup>-2</sup> in the Li/LPSO/Li cell, and 1.36 mA cm<sup>-2</sup> in the case of Li/LPSON/Li. Those observations indicate the SEI turns from a nonreactive, protective interphase to a reactive layer when cycling the cells above those current densities. Since the LPSON GSE shows a higher CCD at high temperature, long cycling at different current densities was then investigated in the Li/LPSON/Li cell. Figure 7(C) shows short-circuiting at 2 mA cm<sup>-2</sup> after cycling for 320 hours.

### Effects of LM Foil – GSE SEIs

Unlike the pressed pellet form of GSEs, the bulk glass sample pieces are tested in coin cells, which do not have a high applied pressure throughout the whole testing time as in the die cells. Due to the technique limitations, the glass surfaces which are polished by hand are not strictly parallel. Defects such as bubbles and scratches formed by the polishing papers are also observed on the surfaces, which will lead to difficulty in the lithium wetting. Therefore, the contact of lithium with the GSE is always our concern. To simulate the environment in the coin cell, the Li/GSE components were placed in a die cell, and parallel pressure was applied on both sides of the laminations. Figure S4 shows the Li/GSE components after pressing for 5 min, the majority part of GSE has contact with the LM foil, however, there are still void areas. To solve this problem, we used thin LM foils and carefully pressed the LM foil onto the glass surface with a stainless-steel cylinder, and this method shows a much better wetting for the whole LM to SE area. Another important factor is the LM surface; even though the as-purchased LM foils are clean in visual inspection, there is still a contaminated layer that causes a large interfacial resistance. To decrease the interfacial resistance, the surface of the LM foil was removed before each use, and the interfacial resistance was decreased dramatically (Figure S5). In summary, the LM needs to be cleaned before each use to provide a good contact.

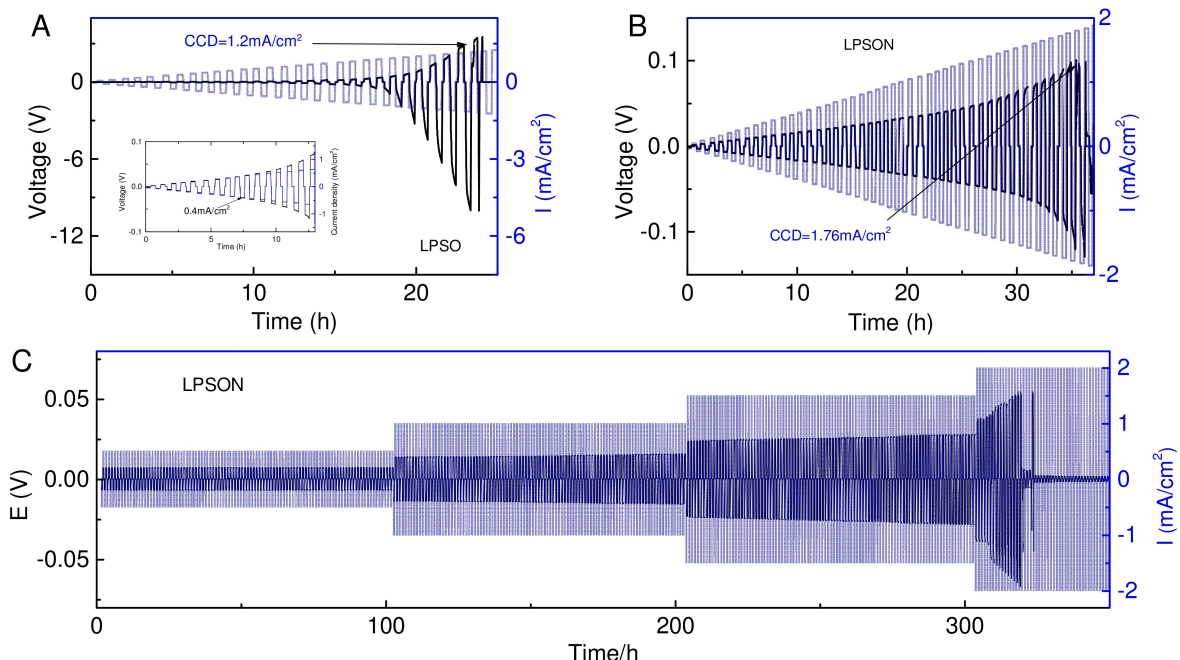


**Figure 7.** Galvanostatic cycling of the Li/GSE/Li symmetric cells at step-increased current densities at 100 °C of A) LPSO, B) LPSON. The time for each step is 20 min; the current intensity step size is 0.04 mA cm<sup>-2</sup>. C) Voltage profiles of Li/LPSON/Li cell at 0.5 mA cm<sup>-2</sup> for 100 cycles, 1 mA cm<sup>-2</sup> for 100 cycles, 1.5 mA cm<sup>-2</sup> for 100 cycles, and then cycled at 2 mA cm<sup>-2</sup> until short, the time for each charge/discharge is 20 min.

## Conclusion

In conclusion, three different GSEs: LPS 0.6 Li<sub>2</sub>S + 0.4(0.8 SiS<sub>2</sub> + 0.2 P<sub>2</sub>S<sub>5</sub>), LPSO 0.67 Li<sub>2</sub>S + 0.33(0.8 SiS<sub>2</sub> + 0.2 P<sub>2</sub>O<sub>5</sub>) and LPSON 0.95(0.67 Li<sub>2</sub>S + 0.264 SiS<sub>2</sub> + 0.066 P<sub>2</sub>O<sub>5</sub>) + 0.05(LiPO<sub>2.20</sub>N<sub>0.54</sub>) were successfully synthesized by the MQ method, and their SRO structures, thermal properties, and electrochemical properties were examined to investigate the effects of O and N doping on the base pure sulfide LPS GSE. As P<sub>2</sub>O<sub>5</sub> is added to the glass, the defect P<sup>1P</sup> units convert to normal P<sup>1</sup>(P<sub>2</sub>S<sub>7</sub><sup>4-</sup>) SRO units and Si<sup>1</sup> SRO units disappear in the LPSO glass. An anion exchange between P and Si is also observed such that the original Si—S bonds in the starting material SiS<sub>2</sub> change from Si—S to Si—O and concomitantly, the original P—O bonds in the P<sub>2</sub>O<sub>5</sub> starting material change from P—O to P—S bonds. Both networking, BOs and BSs units, and non-networking, NBOs and NBSs, oxy-sulfide P and Si species were determined using <sup>31</sup>P and <sup>29</sup>Si MAS NMR and confirmed the existence of P<sup>2</sup>(PS<sub>2</sub>O<sup>-</sup>) SRO units and SiO<sub>4-x</sub>S<sub>x</sub> units ( $x=0, 1, 2$ , and 3). While not fully determined at this point, we believe these Si SRO units are comprised of more polymerized Si<sup>2</sup> and Si<sup>3</sup> SRO possessing increasing numbers of BOs and BSs. Work is in progress to fully identify the exact nature of these units. Raman peaks centered at 440 and 656 cm<sup>-1</sup> were assigned to BOs with Si and P, respectively. Characteristic peaks associated with NBOs were observed in the high wavenumber region of the Raman spectra. Due to the small doping amount of N, no new peaks associated with nitrogen were observed in either the NMR or Raman spectra of the LiPON doped LPSO. However, the presence of doubly bonded N<sub>d</sub> species was confirmed in the XPS spectra of LPSON GSE. Significant changes of the  $T_g$  and  $T_c$  are observed between the three samples, which is evidence of the successful incorporation of O and N in the structure. No silicon ejection was observed in all MQ glasses, which is quite common in thiosilicate-based PBM GSEs, indicating that the MQ synthesis method is an advantageous method of producing these GSEs.

According to the electrochemical characterization, the LPS GSE showed the highest CCD, however, the SEI between the GSE and lithium is not stable, and keeps growing throughout the whole test, which makes LPS impossible to be used in practice as a low-cost SE without further surface modification. Upon oxygen doping, the stability of the SEI between LM and the LPSO GSE greatly improved, and a CCD of 0.48 mA cm<sup>-2</sup> at room temperature was achieved, however, the interphase showed activity at high current densities. Finally, the SEI of the LPSON GSE with LM was non-reactive and stable at room temperature with a CCD of 0.48 mA cm<sup>-2</sup>. Our results suggest that the preferential formation of new Si—O bonds with added O and the preferential formation of new P—N bonds leads to the dramatically improved electrochemical stability of the LPSON GSE over LPSO and LPS GSEs. It should be noted that there is still potential to further increase the CCD of LPSON.

Another application of these GSE is in high temperature batteries, or in higher temperature operation. LPSO and LPSON were tested in LM symmetric cells at 100°C. Improved CCDs of 1.2 and 1.76 mA cm<sup>-2</sup> were observed for LPSO and LPSON cells, respectively. However, when cycling the cells at CDs higher

than 0.4 and 1.36 mA cm<sup>-2</sup>, the interphase starts to show reactivity, which means to achieve a high CCD and long stable cycling at high temperature, the glass composition and structure needs to be further optimized. To our knowledge, our work is the first to report the electrochemical properties of the oxygen and nitrogen doped GSE compositions in grain-boundary-free form. We believe our new report here will provide guidance to the design and development of superior grain-boundary free GSEs.

## Experimental Section

### Synthesis of MQ bulk glass pieces

All of the GSEs were produced via MQ technique inside a nitrogen glovebox with < 2 ppm H<sub>2</sub>O and O<sub>2</sub>.

### 0.6 Li<sub>2</sub>S + 0.4(0.8 SiS<sub>2</sub> + 0.2 P<sub>2</sub>S<sub>5</sub>) MQ glass (LPS)

Phosphorus sulfide (P<sub>2</sub>S<sub>5</sub>, 98% Acros Organics) and lithium sulfide (Li<sub>2</sub>S, 99.9% Alfa Aesar) were used as received. Silicon sulfide, SiS<sub>2</sub>, was prepared in-house by reacting elemental silicon (99.999%, Alfa Aesar) and sulfur (99.999% Acros Organics) in a sealed and evacuated, ~4 Pa, ampoule at high temperature.<sup>[65]</sup> The raw materials were weighed in stoichiometric amounts to make 5-gram samples, mixed for 10 min using a SpexMill 8100, and melted in a covered vitreous carbon crucible at temperatures ranging from 780 to 900°C. LPS was melted for 6 minutes two times, first to check for mass loss during melting and second to cast the molten glass charge as small disc, typically 1–2 mm thick × 10–14 mm diameter. Mass losses of less than 2% were observed for all of the compositions prepared. To relieve residual internal stresses introduced during casting and quenching of the melt, the liquid was quenched between brass plates heated to 30°C below the glass transition temperature ( $T_g$ ), allowed to anneal overnight, and then cooled at 1 °C/min to 25 °C.

### 0.67 Li<sub>2</sub>S + 0.33(0.8 SiS<sub>2</sub> + 0.2 P<sub>2</sub>O<sub>5</sub>) MQ glass (LPSO)

The synthesis procedure for the composition 0.67 Li<sub>2</sub>S + 0.264 SiS<sub>2</sub> + 0.066 P<sub>2</sub>O<sub>5</sub> (LPSO) was identical to the procedure of LPS. Instead of phosphorus sulfide, phosphorus pentoxide (P<sub>2</sub>O<sub>5</sub>, 99.95% Fisher Scientific) was mixed with lithium sulfide and silicon sulfide according to the stoichiometry, and then melt-quenched after mixing using a SpexMill 8100 for 10 min, followed by annealing for 3 hr and cooled to room temperature at the same cooling rate.

### 0.95(0.67 Li<sub>2</sub>S + 0.264 SiS<sub>2</sub> + 0.066 P<sub>2</sub>O<sub>5</sub>) + 0.05(LiPO<sub>2.20</sub>N<sub>0.54</sub>) MQ glass (LPSON)

The LPSON GSE with nitrogen was produced by remelting appropriate amounts of LPSO GSE and the oxynitride glass LiPO<sub>2.20</sub>N<sub>0.54</sub>(LiPON). LiPON was prepared by melting LiPO<sub>3</sub> glass at 780°C under a constant NH<sub>3</sub> flow.<sup>[53]</sup> LPSO and LiPON glasses were weighed in stoichiometric amounts to make 5-gram samples inside the N<sub>2</sub>-filled glovebox, mixed for 10 min using a SpexMill 8100, and melted in a covered vitreous carbon crucible at temperatures ranging from 780 to 900°C. LPSON was melted for 6 minutes two times to check for mass loss during melting, and a mass loss of less than 2% was found. After the second melting, the liquid was quenched between brass plates heated to 30°C below  $T_g$ , allowed to anneal for 3 hr, and then cooled at 1 °C/min to 25 °C.

## Material characterization

Powder X-ray diffraction (PXRD), scanning electron microscopy (SEM), X-ray photoelectron spectroscopy (XPS), Raman spectroscopy and nuclear magnetic resonance spectroscopy (NMR) were used to perform structural and chemical characterizations of the MQ glasses, while differential scanning calorimetry (DSC) was used to determine the thermal properties of the glasses.

A Rigaku SmartLab X-ray Diffractometer equipped with a copper anode of 40 kV and 44 mA was used to confirm the amorphous nature of the glasses. A  $0.01^\circ$  step size and  $1^\circ/\text{min}$  scan rate were used with a  $2\theta$  range from  $10^\circ$  to  $70^\circ$ . All the MQ samples were tested after polishing the surface. The samples were placed on a zero-background single crystal silicon wafer inside an airtight sample holder.

SEM imaging was performed using an XL 30 ESEM-FEG microscope and a 5 kV electron beam. The glasses were placed into an environmental mini-chamber designed for the transport of air-sensitive samples, which can be opened when the SEM chamber is evacuated.

XPS was performed on a Kratos Amicus/ESCA 3400 with an Mg anode operating under 240 W and 12 kV. Samples were transferred with an air sensitive sample holder. The photoelectrons were emitted at  $0^\circ$  with a spot size of 3 mm, and were analyzed with a DuPont type analyzer. A pass energy of 150 eV was used for high-resolution spectra. The spectra were calibrated to the hydrocarbon peak at 284.5 eV. Peak fitting was performed using CasaXPS processing software.

A Renishaw inVia Raman spectrometer utilizing a 20 mW 488 nm Argon laser scanning between 150 to  $1250 \text{ cm}^{-1}$  was used to collect the Raman spectra. Glass samples were sealed in an airtight optically transparent sample holder to prevent oxygen and moisture contamination during measurements.

To prepare samples for NMR measurements, adventitious contamination on the glass surface was removed by polishing, and then the finely ground samples were packed into 4 mm zirconia rotors inside an Ar-filled glovebox with  $< 0.1 \text{ ppm H}_2\text{O}$  and  $\text{O}_2$ . The  $^{31}\text{P}$  MAS NMR spectra were collected using a pulse-acquire sequence performed at 242.94 MHz on a 600 MHz Bruker spectrometer equipped with a triple-resonance (HXY) probe. The rotor was spun at 12.5 kHz, and 96 transient measurements were collected using a recycle delay of 300 s. The  $^{29}\text{Si}$  MAS NMR measurements were performed using a pulse-acquire sequence at 79.49 MHz on a 400 MHz Bruker spectrometer equipped with a double resonance (HX) probe. The rotor was spun at 10 kHz, and spectra were composed of 4000–6000 transient measurements collected using a recycle delay of 45 s. The  $^{31}\text{P}$  and  $^{29}\text{Si}$  spectra were indirectly referenced to the  $^1\text{H}$  signal of TMSS following the procedure described by Harris et al.<sup>[66]</sup>

A Perkin-Elmer Pyris Diamond differential scanning calorimeter (DSC) was used to determine the glass transition temperature,  $T_g$ , of the glasses. Bulk small chunk samples of 8–10 mg were packed and hermetically sealed inside 25  $\mu\text{L}$  aluminum pans inside a  $\text{N}_2$  glove box. The samples were heated from  $50^\circ\text{C}$  to  $400^\circ\text{C}$  at  $20^\circ\text{C}/\text{min}$  to determine  $T_g$  and the crystallization temperature,  $T_c$ , using the onset method. A second set of cycle scans were performed on a freshly prepared sample by heating from  $50^\circ\text{C}$  to  $20$ – $30^\circ\text{C}$  above the  $T_g$ , but below  $T_c$ , and cooled to  $150^\circ\text{C}$  which was repeated two times to measure the  $T_g$  with an established thermal history. On the final scan, the sample was heated to  $400^\circ\text{C}$  to determine the  $T_g$  and the  $T_c$  after the post thermal cycling. Herein, the last scan was used to determine  $T_g$  and  $T_c$  of the glasses that had undergone the post-formation stress relaxation.

## Electrochemical characterization

All of the electrochemical measurements were conducted using a VMP-300 Biologic potentiostat/galvanostat. Glasses were polished with micro-polishing papers down to  $\sim 1 \mu\text{m}$  and then used directly; coin cells were assembled and sealed in an Ar-filled glove box and tested outside the glovebox.

EIS measurements were performed on symmetric cells using clean LM foils as non-blocking electrodes. LM foils were polished and rolled into thin pieces before use. The frequency range was from 100 Hz to 3 MHz using a 10 mV stimulus voltage. To investigate the stability in contact with LM, EIS profiles were collected every 0.5 hour for 9.5 hours. After the EIS measurements, CCD measurements were performed using a series of increasing CDs with a step size of  $0.05 \text{ mA/cm}^2$ , and a cycle time of 40 min for each charge/discharge cycle, until the cell failed due to the LD penetration.

To investigate the reaction voltage of the GSEs and LM, cyclic voltammetry (CV) was conducted on an asymmetric cell with a structure of Li/GSEs/stainless steel. The cell was scanned from 0 to 4 V and  $-0.5$  to 5 V with a scan rate of  $1 \text{ mV s}^{-1}$ .

## Supporting Information

Supporting Information is available from the Wiley Online Library or from the author.

## Acknowledgements

This work was supported by contracts DE-AR000654 and DE-AR000778 through the ARPA-E, by contract DE-EE0008852 through the EERE Vehicular Technologies Office, and by the NSF by grant NSF-DMR 1936913. All authors have given approval to the final version of the manuscript. Dr. Dapeng Jing is gratefully acknowledged for his help in collecting the XPS data reported in this paper. Open Access funding provided by the Iowa State University Library.

## Conflict of Interest

The authors declare no conflict of interest.

**Keywords:** grain-boundary-free · lithium battery · mixed glass former · solid state electrolyte · sulfide glass

- [1] M. Ribes, B. Barrau, J. L. Souquet, *J. Non-Cryst. Solids* **1980**, *38*–*39*, 271.
- [2] B. Barrau, M. Ribes, M. Maurin, A. Kone, J. L. Souquet, *J. Non-Cryst. Solids* **1980**, *37*, 1.
- [3] A. Levasseur, J. C. Brethous, J. M. Reau, P. Hagenmuller, M. Couzi, *Solid State Ionics* **1980**, *1*, 177–86.
- [4] J. P. Malugani, G. Robert, *Solid State Ionics* **1980**, *1*, 519.
- [5] K.-H. Kim, S. W. Martin, *Chem. Mater.* **2019**, *31*, 3984.
- [6] N. Kamaya, K. Homma, Y. Yamakawa, M. Hirayama, R. Kanno, M. Yonemura, T. Kamiyama, Y. Kato, S. Hama, K. Kawamoto, A. Mitsui, *Nat. Mater.* **2011**, *10*, 682.
- [7] Y. Kato, S. Hori, T. Saito, K. Suzuki, M. Hirayama, A. Mitsui, M. Yonemura, H. Iba, R. Kanno, *Nat. Energy* **2016**, *1*, 16030.
- [8] J. Fu, *Solid State Ionics* **1997**, *96*, 195.
- [9] J. Fu, *Solid State Ionics* **1997**, *104*, 191.

- [10] A. Hayashi, K.-I. Minami, M. Tatsumisago, *J. Solid State Electrochem.* **2010**, *14*, 1761.
- [11] F. Mizuno, A. Hayashi, K. Tadanaga, T. Minami, M. Tatsumisago, *Solid State Ionics* **2004**, *175*, 699.
- [12] K. Kaup, J. D. Bazak, S. H. Vajargah, X. Wu, J. Kulisch, G. R. Goward, L. F. Nazar, *Adv. Energy Mater.* **2020**, *10*, 1902783.
- [13] L. Porz, T. Swamy, B. W. Sheldon, D. Rettenwander, T. Froemling, H. L. Thaman, S. Berendts, R. Uecker, W. C. Carter, Y.-M. Chiang, *Adv. Energy Mater.* **2017**, *7*, 1701003.
- [14] Y. Ren, Y. Shen, Y. Lin, C.-W. Nan, *Electrochem. Commun.* **2015**, *57*, 27.
- [15] F. Aguesse, W. Manalastas, L. Buannic, J. M. Lopez del Amo, G. Singh, A. Llordés, J. Kilner, *ACS Appl. Mater. Interfaces* **2017**, *9*, 3808.
- [16] R. Garcia-Mendez, F. Mizuno, R. Zhang, T. S. Arthur, J. Sakamoto, *Electrochim. Acta* **2017**, *237*, 144.
- [17] R. Prasada Rao, M. Seshasayee, *J. Non-Cryst. Solids* **2006**, *352*, 3310.
- [18] T. Ohtomo, F. Mizuno, A. Hayashi, K. Tadanaga, M. Tatsumisago, *Solid State Ionics* **2005**, *176*, 2349.
- [19] A. Hayashi, T. Konishi, K. Tadanaga, T. Minami, M. Tatsumisago, *J. Power Sources* **2005**, *146*, 496.
- [20] F. Mizuno, A. Hayashi, K. Tadanaga, M. Tatsumisago, *Adv. Mater.* **2005**, *17*, 918.
- [21] J. H. Kennedy, *Mater. Chem. Phys.* **1989**, *23*, 29–50.
- [22] J. H. Kennedy, S. Sahami, S. W. Shea, Z. Zhang, *Solid State Ionics* **1986**, *18*–19, 368.
- [23] S. Sahami, S. W. Shea, J. H. Kennedy, *J. Electrochem. Soc.* **1985**, *132*, 985.
- [24] F. Han, Y. Zhu, X. He, Y. Mo, C. Wang, *Adv. Energy Mater.* **2016**, *6*, 1501590.
- [25] Y. Zhu, X. He, Y. Mo, *ACS Appl. Mater. Interfaces* **2015**, *7*, 23685.
- [26] Y. Li, W. Zhou, X. Chen, X. Lü, Z. Cui, S. Xin, L. Xue, Q. Jia, J. B. Goodenough, *Proc. Natl. Acad. Sci. USA* **2016**, *113*, 13313.
- [27] X. Han, Y. Gong, K. K. Fu, X. He, G. T. Hitz, J. Dai, A. Pearse, B. Liu, H. Wang, G. Rubloff, Y. Mo, V. Thangadurai, E. D. Wachsman, L. Hu, *Nat. Mater.* **2017**, *16*, 572.
- [28] W. Zhou, Y. Li, S. Xin, J. B. Goodenough, *ACS Cent. Sci.* **2017**, *3*, 52.
- [29] K. Fu, Y. Gong, B. Liu, Y. Zhu, S. Xu, Y. Yao, W. Luo, C. Wang, D. Lacey Steven, J. Dai, Y. Chen, Y. Mo, E. Wachsman, L. Hu, *Sci. Adv.* **2017**, *3*, e1601659.
- [30] A. Rabenau, *Solid State Ionics* **1982**, *6*, 277.
- [31] N. Aotani, K. Iwamoto, K. Takada, S. Kondo, *Solid State Ionics* **1994**, *68*, 35.
- [32] K. Iio, A. Hayashi, H. Morimoto, M. Tatsumisago, T. Minami, *Chem. Mater.* **2002**, *14*, 2444.
- [33] R. Sakamoto, M. Tatsumisago, T. Minami, *J. Phys. Chem. B* **1999**, *103*, 4029.
- [34] R. Zhao, S. Kmiec, G. Hu, S. W. Martin, *ACS Appl. Mater. Interfaces* **2020**, *12*, 2327.
- [35] R. Zhao, G. Hu, S. Kmiec, R. Gebhardt, A. Whale, J. Wheaton, S. W. Martin, *ACS Appl. Mater. Interfaces* **2021**, *13*, 26841.
- [36] S. Kmiec, A. Joyce, D. Bayko, S. W. Martin, *J. Non-Cryst. Solids* **2020**, *534*, 119776.
- [37] S. Kmiec, A. Joyce, S. W. Martin, *J. Non-Cryst. Solids* **2018**, *498*, 177.
- [38] S. S. Berbano, I. Seo, C. M. Bischoff, K. E. Schuller, S. W. Martin, *J. Non-Cryst. Solids* **2012**, *358*, 93.
- [39] D. E. Watson, S. W. Martin, *J. Non-Cryst. Solids* **2017**, *471*, 39.
- [40] D. E. Watson, S. W. Martin, *Inorg. Chem.* **2018**, *57*, 72.
- [41] R. J. Hemley, H. K. Mao, P. M. Bell, B. O. Mysen, *Phys. Rev. Lett.* **1986**, *57*, 747.
- [42] A. K. Yadav, P. Singh, *RSC Adv.* **2015**, *5*, 67583.
- [43] C. Dietrich, D. A. Weber, S. J. Sedlmaier, S. Idris, S. P. Culver, D. Walter, J. Janek, W. G. Zeier, *J. Mater. Chem. A* **2017**, *5*, 18111.
- [44] A. Hayashi, K. Tadanaga, M. Tatsumisago, T. Minami, Y. Miura, *J. Ceram. Soc. Jpn.* **1999**, *107*, 510.
- [45] K. Hirai, M. Tatsumisago, M. Takahashi, T. Minami, *J. Am. Ceram. Soc.* **1996**, *79*, 349.
- [46] S. J. Kmiec, J. M. Lovi, A. Joyce, D. Bayko, S. W. Martin, *J. Non-Cryst. Solids* **2021**, *553*, 120493.
- [47] H. Eckert, J. H. Kennedy, A. Pradel, M. Ribes, *J. Non-Cryst. Solids* **1989**, *113*, 287–93.
- [48] A. Pradel, G. Taillades, M. Ribes, H. Eckert, *J. Non-Cryst. Solids* **1995**, *188*, 75.
- [49] H. Eckert, J. H. Kennedy, A. Pradel, M. Ribes, *J. Non-Cryst. Solids* **1989**, *13*, 287.
- [50] A. Pradel, A. Piarristeguy, *C. R. Geosci.* **2022**, *354*, 1.
- [51] M. Tatsumisago, *J. Ceram. Soc. Jpn.* **2001**, *109*, 809.
- [52] M. Tatsumisago, H. Morimoto, H. Yamashita, T. Minami, *Solid State Ionics* **2000**, *136*–137, 483.
- [53] J. E. De Souza, S. Rojas De Souza, R. Gebhardt, S. Kmiec, A. Whale, S. Warthen Martin, *Int. J. Appl. Glass Sci.* **2020**, *11*, 78–86.
- [54] S. Wenzel, S. J. Sedlmaier, C. Dietrich, W. G. Zeier, J. Janek, *Solid State Ionics* **2018**, *318*, 102.
- [55] B. Fleutot, B. Pecquenard, H. Martinez, M. Letellier, A. Levasseur, *Solid State Ionics* **2011**, *186*, 29.
- [56] A. Hayashi, H. Yamashita, M. Tatsumisago, T. Minami, *Solid State Ionics* **2002**, *148*, 381.
- [57] A. Hayashi, R. Komiya, M. Tatsumisago, T. Minami, *Solid State Ionics* **2002**, *152*–153, 285.
- [58] T. Yamada, S. Ito, R. Omoda, T. Watanabe, Y. Aihara, M. Agostini, U. Ulissi, J. Hassoun, B. Scrosati, *J. Electrochem. Soc.* **2015**, *162*, A646.
- [59] F. Han, T. Gao, Y. Zhu, K. J. Gaskell, C. Wang, *Adv. Mater.* **2015**, *27*, 3473.
- [60] S. Wenzel, D. Weber, T. Leichtweiss, M. Busche, J. Sann, J. Janek, *Solid State Ionics* **2016**, *286*, 24.
- [61] J. H. Kennedy, Z. Zhang, *J. Electrochem. Soc.* **1989**, *136*, 2441–3.
- [62] W. Wan, Q. Zhang, Y. Cui, E. Wang, *J. Phys. Condens. Matter* **2010**, *22*, 415501.
- [63] T. Kim, S. Park, S. M. Oh, *J. Electrochem. Soc.* **2007**, *154*, A1112.
- [64] J. B. Bates, G. R. Gruzalski, N. J. Dudney, C. F. Luck, X. Yu, *Solid State Ionics* **1994**, *70*–71, 619.
- [65] M. Tenhover, M. A. Hazle, R. K. Grasselli, *Phys. Rev. Lett.* **1983**, *51*, 404.
- [66] R. K. Harris, E. D. Becker, S. M. Cabral de Menezes, R. Goodfellow, P. Granger, *Solid State Nucl. Magn. Reson.* **2002**, *22*, 458.

Manuscript received: November 22, 2021

Revised manuscript received: August 17, 2022

Accepted manuscript online: August 18, 2022

Version of record online: September 22, 2022